

Northridge Earthquake Rupture Models Based on the Global Positioning System Measurements

by Zheng-Kang Shen, Bob X. Ge, David D. Jackson, David Potter, Michael Cline, and Li-yu Sung

Abstract We use global positioning system (GPS) data to study the rupture mechanism of the 1994 Northridge earthquake in southern California. We include data from 62 observation sites, of which two (Palos Verdes and Jet Propulsion Lab) are permanent GPS geodetic array (PGGA) sites. We use a grid-search scheme to study the range of single- and dual-plane, uniform and varied slip models consistent with the data. We find that in order to fit the geodetic data with a fault model whose primary fault patch is confined to a plane through the aftershocks, a secondary fault plane is required above the primary fault plane. The moment release of the secondary fault can be as large as 1.9×10^{18} N-m, 14% of the moment release of the primary fault. This result implies significant deformation in the shallow crust associated with the mainshock. Our preferred model has a 14×14 array of dislocation patches on a plane through the main aftershock cluster and a 5×6 array of patches in the hanging wall west of the epicenter. We estimate the displacements on the patches by linear inversion with a first-order smoothness constraint. The estimated displacements on the main fault for this model are confined to a simple region between depths of 5 and 18 km, in the interior of the modeled fault surface. The mainshock lies at the bottom of the aftershock zone, near which about 1-m slip is shown on our modeled fault surface. The maximum slip on the fault surface is about 2.2 m, located at 34.28° N, 118.55° W, and 12.4 km at depth. The seismic moment release estimate of $1.34 \pm 0.15 \times 10^{19}$ N-m on the main fault at the 95% confidence is consistent with the estimate from strong-motion studies.

Introduction

The 17 January 1994 Northridge earthquake occurred in the San Fernando Valley, California, a densely populated suburb of the Los Angeles metropolitan area. The San Fernando Valley is in the central Transverse Ranges and is surrounded by Holocene faults: The Santa Susana fault lies north, the Sierra Madre fault west, and the Santa Monica fault south. Active tectonic deformation has been detected in the valley and its vicinity. A 1 to 4 mm/yr convergence across the valley was detected geodetically (Shen *et al.*, 1995). Geological studies showed N–S shortening at a rate of 3.8 to 6.8 mm/yr in the Los Angeles Basin east of the valley and 2.5 to 5.2 mm/yr across the Elysian Park thrust along the eastern portion of the Santa Monica Mountains anticlinorium (Davis *et al.*, 1989), possibly accompanied by blind thrusting and decollement in the lower crust. Northwest of the valley, GPS studies by Donnellan *et al.* (1993a) estimated the N–S shortening of the Ventura Basin at a rate of 7 to 10 mm/yr, which was matched by a revised geological estimate by Yeats (1993). According to Yeats and Hufnagle (1995), the Northridge earthquake probably ruptured an extension of the Oak Ridge fault, a south-dipping reverse

fault at the southern boundary of the Ventura Basin. Thus, the shortening detected in the Ventura Basin probably extends into the valley, accomplished partly by the north-dipping Santa Susana fault responsible for the 1971 Sylmar earthquake and the south-dipping “Northridge” fault. Studies by Davis and Namson (1994) placed 1.4- to 1.7-mm/yr slip at the location of the previously unknown Northridge fault.

The focal mechanism is generally well resolved by seismic data, but nevertheless, significant variations among the earthquake source parameters result from using different data and/or different methods: depth estimates range from 10 to 19 km, strike from 113° to 136° , dip from 30° to 62° , and seismic moment from 1.1 to 2.1×10^{19} N-m (Jones *et al.*, 1994; Song *et al.*, 1994; Thio and Kanamori, 1994; Wald *et al.*, this issue; Zhang *et al.*, 1994; Dreger, 1994; Zhao, 1994). These ranges are not surprising because the results were derived from different period ranges of the seismic signals. At the very low frequency end, geodetic studies can help determine the size, location, and final rupture of the fault plane, as well as possible anelastic deformation asso-

anelastic deformation in the epicentral area caused by strong co-seismic shaking may also have important contributions to the error spectrum. A thorough error analysis is rather difficult. Here we adopt an *ad hoc* uncertainty formula to accommodate the intrinsic as well as the nontectonic errors:

$$\sigma_i = (\sigma_i'^2 + c_i^2 + (D_i/D_0)^2)^{1/2}$$

where σ_i' is the formal uncertainty from the GLOBK inversion; c_i is a constant to accommodate errors, such as unmodeled aseismic corrections; D_i/D_0 represents unmodeled near-field anelastic displacements; D_0 is a constant; and D_i is the amplitude of the co-seismic displacement in millimeters for that site. We take $c_i = 3$ mm for horizontal components and 10 mm for vertical components, and $D_0 = 30$. Figures 2 and 3 respectively show the horizontal and the vertical co-seismic displacements solved along with their error ellipses representing one standard deviation.

We have also done some editing of the data. We omit

stations NORT and LOVE because we do not trust their monument stability, and we suspect nontectonic displacements there (see Hudnut *et al.*, this issue, for details of the problems). We also omit stations 0705 and PEAR. These two sites are located northeast of the San Andreas fault, their secular displacement corrections are much larger than those of the other sites, and the errors of their corrections may be comparable to the signals themselves. We assign a large uncertainty (40 mm) to the vertical displacement of station CATO, because this measurement may have been contaminated by an antenna height measurement error (also see Hudnut *et al.*, this issue). The rest of the solutions we use are the same as those in Table 1 of Hudnut *et al.* (this issue). We use JPLB as our reference station.

Uniform Slip Dislocation Models

Uniform Single Patch

To begin with, we adopt a rectangular, uniform dislocation fault model (Okada, 1985) in a homogeneous elastic

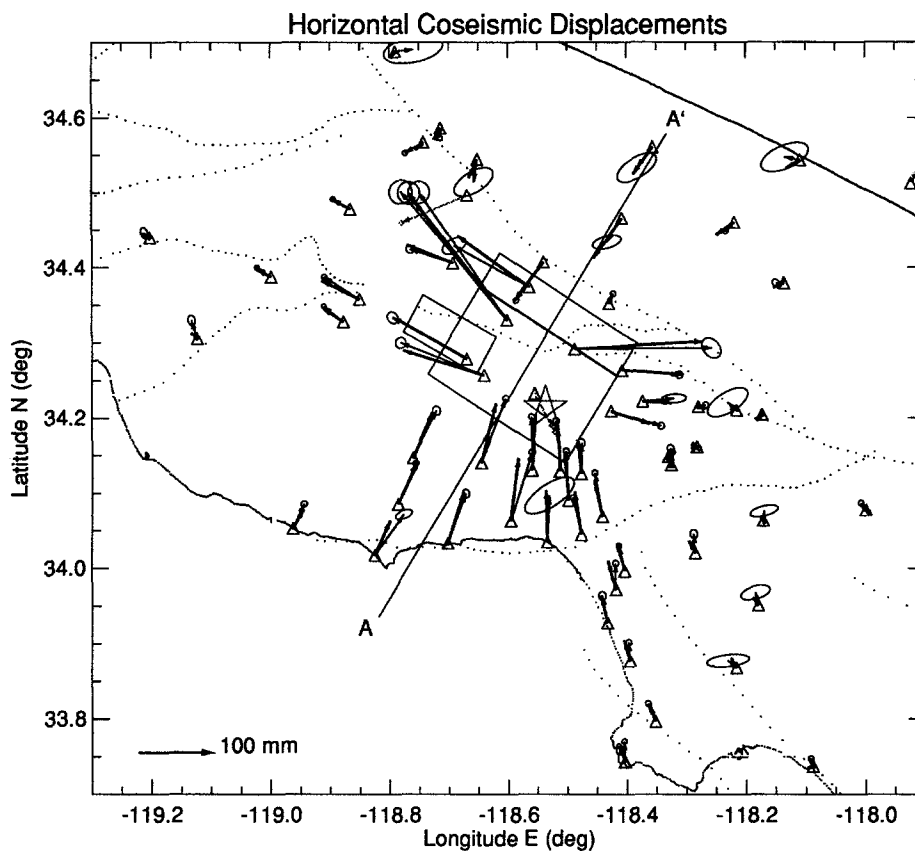


Figure 2. Horizontal co-seismic displacements. The thin arrows with error ellipses are the data measured by GPS. The error ellipses show one standard deviation. The thick arrows without error ellipses are the predicted displacements by a dual-plane varied slip fault model (model F), described later. Measured station displacements not used in this study are shown by gray arrows. The earthquake epicenter is shown by a star. The large rectangle covering the epicenter illustrates the map view of a fault plane for a varied slip fault model (model E). The dividing line in the rectangle is the hinge line of the model. This rectangle and the other small rectangle are the fault planes for model F.

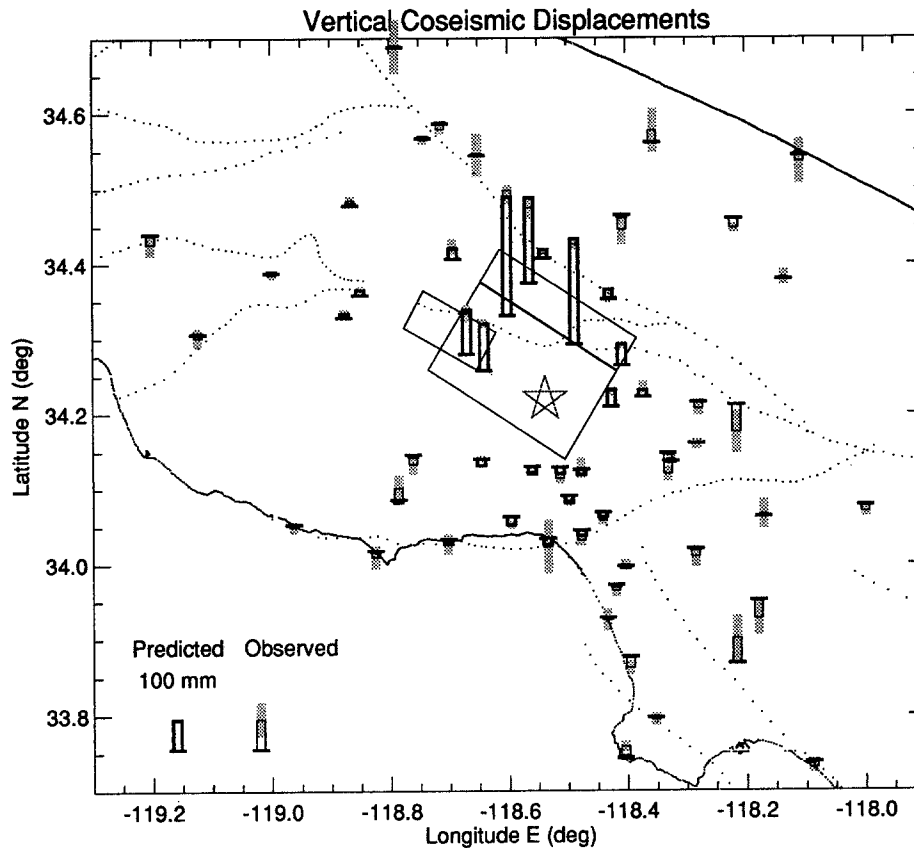


Figure 3. Vertical co-seismic displacements. Horizontal dash bars denote the station locations and the zero lines of the vertical displacements. Data are illustrated by columns with thin outlines, with the shaded columns showing one standard deviation uncertainties. The columns with thick outlines are the data predicted by model F.

half-space. The Poisson ratio of the elastic half-space is assumed to be 0.23. Nine parameters describe the model: latitude and longitude of the center, horizontal length, top depth, bottom depth, strike and dip of the patch, horizontal slip, and updip slip on the fault patch. The observed displacements on the earth's surface are nonlinear functions of the first seven parameters and linear functions of the slip components. We use the following search procedure to find the set of parameters providing the smallest residual variance:

1. Select an initial value for each nonlinear parameter and an initial step size. Select a second value for each parameter by incrementing the initial value by the step size.
2. For each of the 2^7 possible choices of parameters, estimate the slip components by linear inversion, and compute the residual variance. Record whether the initial or the incremented value of each parameter led to the smallest residual variance. If the initial value was chosen, multiply the step size by -0.6 ; otherwise, leave it the same.
3. For each parameter, again select two values: the winner of the last round and an incremented value.
4. Repeat steps 2 and 3 until residual variance fails to decrease substantially on successive rounds.

The resultant model is what we call model A, whose normalized residual variance is 649.3, corresponding to a normalized root mean square (NRMS) residual of 1.93.

Single Patch through Aftershocks

Model A appears to be a reasonable fit to the data, considering the simplicity of the model, and most of the resolved parameters appear consistent with those obtained from seismological studies. However, a closer look shows that the fault plane does not go through the concentrated aftershocks in the hypocentral region. Figure 4 shows the cross section of the best-searched fault plane along with the projected aftershocks. It appears that the fault plane goes parallel to and about 3 to 4 km above the major aftershock zone, where the co-seismic rupture presumably occurred. To find a model more consistent with the aftershock plane, we make a second trial (model B), in which the rectangular fault patch is forced to go through the plane defined by the configuration of the aftershocks. We allow the four edges of the fault patch to vary in the plane and use the search procedure described above to determine their best estimates along with the two rupture components. This model gives a postfit residual variance of 1304.8, much larger than 649.3 obtained by model A. The F-test shows that model B fits the data worse than

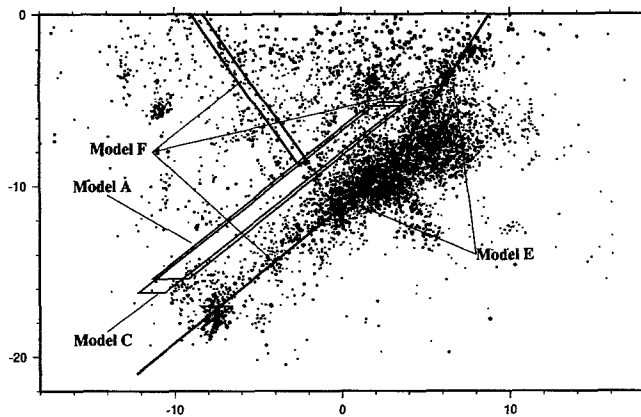


Figure 4. Cross section of the aftershocks and the modeled fault planes. The cross section is oriented $N32.0^\circ E$, normal to the strike direction of model E fault plane, along a profile of A to A' in Figure 2. The aftershock data, shown by dots, are from Mori *et al.* (1995). The fault planes of models E and F are illustrated by thick lines; the fault planes of models A and C are shown by thin lines. The mainshock hypocenter is shown by a star.

model A at the 99% confidence level. Clearly, the data prefer model A to model B. This “fault plane discrepancy” needs more exploration.

We consider several possible causes of the discrepancy. One of them is that the aftershock depths may have been overestimated. A recent study by Zhou (1995) demonstrated that this may happen when a 1D velocity structure model is used to locate earthquakes in a 3D earth. However, the bias is significant only when remote stations are dominantly used for locating the earthquake hypocenters. Here, most stations used for the Northridge aftershock studies were local sites (Mori *et al.*, 1995), so we expect no significant bias.

Single Patch in Layered Half-Space

Another possible explanation of the discrepancy is that the earth model used for dislocation modeling differs from reality, causing biases to the predicted surface displacements. A study by Ekstrom *et al.* (1992) for the 1985 Kettleman Hills earthquake found that a similar discrepancy was considerably reduced when a layered earth model was applied instead of a half-space model. To test this hypothesis, we perform another search using a layered earth model. The earth model is the same as that used by Wald *et al.* (Table 1, this issue) for their strong-motion study of the Northridge earthquake. The surface displacements are calculated using a propagator matrix method (Ward, 1984), by which a point source dislocation is propagated through a layered earth to the surface. A planar rupture surface is approximated by integrating distributed point sources over the rupture plane. The cross section of the best-searched fault plane is also shown in Figure 4. The postfit residual variance of this model (model C) is 718.2, about 10% greater than that of model A. A comparison shows that the fault plane of model

C is about 10% larger than that of model A, but the central location of the fault plane is virtually unchanged. Other tests are made by perturbing the earth media parameters off the values given by Wald *et al.* (this issue), but we do not see significant changes of the central location of the fault plane. Using a layered earth model does not resolve the fault plane discrepancy.

Two Single Patches

Another possible cause of the fault plane discrepancy is that the observed displacements include deformation caused by more than one dislocation source. The mainshock might have triggered immediate rupture on a different fault plane, or aftershocks may have ruptured along a different fault plane, or some aseismic deformation may have occurred after the mainshock and before the GPS measurements. To test this hypothesis, we try a dual-plane dislocation model, with the first rectangular source plane confined to the central plane of the aftershocks and the second source located elsewhere. We apply the search procedure described above to locate the second fault plane and to determine the dimension (four boundaries of the fault plane) of the primary source. The rupture components at the two fault planes are inverted at each search step. Because of the nonlinear nature of the inversion, we perform the complete search several times, with a different initial position of the second fault plane each time. By doing so, we minimize the risk that the final solution falls into a local minimum rather than the global minimum. The second fault plane of model D is found in the hanging wall of the main fault, dip north, strike almost the same as the main fault, and about 4 to 10 km at depth. The residual variance of model D is 366.8, significantly smaller than that of model A. The F-test shows that model D is 99% significantly better than model A. However, model D requires a second fault plane that has about half of the seismic moment as the primary fault plane does, and no special concentration of aftershocks is detected at the location of the second fault plane.

Variable Slip Dislocation Models

Single Fault with Variable Slip

We investigate a mosaic-like fault model to explore the slip variation along the fault plane and to see if a distributed slip would help to solve the fault plane discrepancy. We fix the top depth of a large rectangle at 1 km, the bottom depth at about 22 km, and the length at 30 km and then subdivide the rectangle into 196 congruent patches in a 14×14 grid. We deliberately choose the rectangular region to be larger than the expected rupture surface of the earthquake, with the expectation that the estimated slip would be insignificant near the boundary of the region. This effectively removes the length and top and bottom depths as parameters of the model, so that the constraint above does not really limit the solutions. We constrain the fault plane to have the same fault

center location and the orientation as that of model B, to make sure that the fault plane coincides to the fault rupture plane defined by the aftershocks. In doing so, the inversion becomes linear, and no iteration is needed.

We implement smoothness constraints on the 392 slip parameters in the inversion. The constraints are included in the data equations of the form

$$D_{m+1} - D_m = 0 \pm \sigma_c,$$

where D_m and D_{m+1} are slip components on two adjacent fault patches. One such equation is included for every pair of adjacent patches, for both the horizontal and updip slip components. The smaller the assumed standard deviation σ_c , the greater the weight given to smoothness, the fewer the degrees of freedom resolved by the geodetic data, and the larger the residual sum of squares. We equate the number of degrees of freedom resolved by the data to the trace of the resolution matrix (Jackson, 1979).

To select an adequate smoothness standard deviation σ_c , we do the inversion using different σ_c , ranging from 100 to 5000 mm. We choose the value of 600 mm for σ_c as our best model. Lower values fail to fit the geodetic data adequately, and higher values lead to rather complex models with no substantial improvement in residual variance. The preferred choice of σ_c corresponds to about 26.3 degrees of freedom in the model.

Hinged Single Fault

The aftershock zone seems to change dip at a depth of about 9 km, with the upper panel dipping 20° steeper than the lower panel. In order to see if the dip-angle change has significant effect on the solution, we test a series of models that have the same fault plane configuration below a depth of 9 km but different fault dip above. The two fault panels are connected by a hinge at a depth of 9 km. Our results show that following the aftershock trace for the upper panel does make a difference to the data fitting. The best-fitting model of this type, model E, has a dip-angle change of 20° (dip = 58°) for the upper panel with a postfit residual variance of 383.8, versus 583.2 for the case with no dip-angle change. The fault geometry of model E is demonstrated in Figures 2 and 4. Slip distribution of this model shows that significant slip (>1 m) spans a region of about 15 × 15 km, with the highest slip of 2.6 m centered at a depth of 12 km. The total moment release is 1.41 × 10¹⁹ N-m. The hypocenter of the mainshock is located at the lower east corner of the significant slip zone; the slip at the hypocenter is close to a meter. One noticeable feature is that there is about 0.5- to 0.8-m slip at the northwest top edge of the panel, about a kilometer below station NEWH. This model is in general agreement with the varied slip model of Hudnut *et al.* (this issue).

Hinged Fault Plus Second Fault

Our preferred model includes two fault surfaces: the main fault surface, hinged at a depth of 9.1 km, and a second rectangular fault surface. The main fault surface is subdivided into 196 subfaults, and the second, into 30 subfaults. The geometry of the main fault surface is constrained by the aftershock pattern to the same values used in model E. The strike, dip, latitude, longitude, and depth of the center of the second fault patch are varied for best fit to the data; these are the only nonlinear parameters in the model. We estimate these nonlinear parameters using a grid search, as described above. For each set of values of the nonlinear parameters, we estimate the slip components for all 226 subfaults by linear inversion, including as data the smoothness constraints as described above.

The displacement pattern for the optimum model, which we call model F, is shown in Figure 5. The displacements on the primary fault are rather simple; there is a maximum slip of just over 2 m at a depth of about 12 km, with a regular decrease in slip amplitude with distance away from the maximum. The sense of motion is thrusting of the hanging-wall block on the south over the footwall block on the north. Unlike model E, the preferred model F has no concentration of slip in the upper northwest corner. Instead, this slip is replaced by that on the second fault surface, which is approximately at right angles to the main fault. Slip on the second fault reaches 0.9 m at a depth of 3 km, and the data can be fit best if some slip extends almost to the earth's surface. The seismic moment releases are 1.34 ± 0.06 × 10¹⁹ N-m for the primary fault and 0.19 ± 0.07 × 10¹⁹ N-m for the second fault, respectively. The second fault dips at 52.7° down to the north, with the northeast side thrust up over the southwest. Thus, the second plane has an orientation similar to that of the auxiliary plane of the mainshock focal mechanism. However, the intersection of the second fault plane with the primary is updip and to the north of the hypocenter, and the displacement on the second fault is concentrated about 20 km to the west of the mainshock hypocenter. Still, a wedge of material above both faults is pushed upward to make way for northeast-southwest shortening.

Model F differs from model E only in allowing for displacement on the second fault. The improvement in fit is highly significant, well above the 99% confidence level. Thus the data are fit much better by a model with extra slip concentrated west of the mainshock, within the hanging wall of the mainshock. The surface geology does reveal several faults in the area of our inferred second fault (for example, Yeats and Huftile, 1995), although we do not associate our inferred second fault with a particular named fault. The faulting in the area is quite complex, and our "second" fault may actually represent more than one. In fact, the solution for the second fault is far from unique. An alternate solution has the second fault plane parallel to the primary fault plane and centered in the same place as the second fault in model F. This alternate solution fits the data almost as well as model

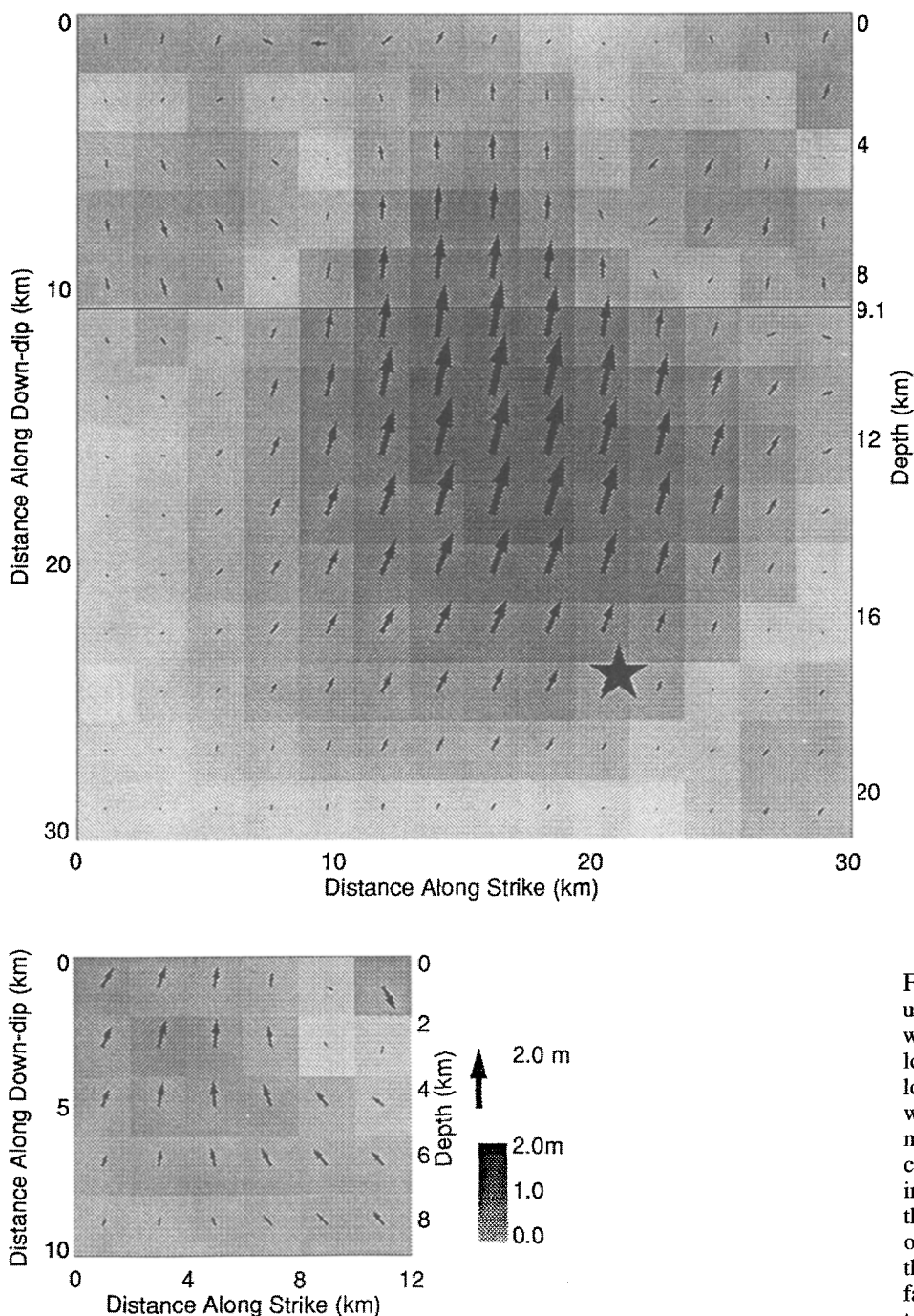


Figure 5. Slip distribution of model F. The upper square shows a 30 by 30 km hinged surface with strike 122.0° and dip south 38.0° for the lower panel and 58.0° for the upper panel. The lower rectangle shows the second fault plane, which strikes 119.3° and dips 52.7° north. Their map projections are shown in Figure 2, and their cross sections are projected in Figure 4. Arrows indicate the slip vectors on the two fault planes, the first fault has 14×14 patches, and the second one has 5×6 patches. The amplitudes of the slips are also shown by the gray scale on the fault patches. The seismic determined hypocenter is shown by a star on the plane.

F. In essence, our results require some inelastic deformation in the hanging wall, but the data cannot resolve it in detail.

Figure 6 shows the resolution of the slip vectors. The resolution for both strike and dip components ranges from above 20% at the top of the hinged fault plane to below 2% at the bottom. Such patterns suggest that slip is better resolved at the top, and the averaging effect is less significant at the top than at the bottom. The smoothness constraints are very important to the final solution; of 452 parameters, the GPS data resolve 31.6, and the smoothness constraints resolve 420.4. The total degree of freedom of model F in Table

1 is different from that given here, because the former includes the nonlinear parameters. Normal slips up to half a meter near the east and west end of the hinged fault at depths of 7 to 9 km should be discounted because of their limited resolution. The resolution for the second fault ranges from above 40% at the northeast corner to below 5% at the bottom. However, the resolution for the second fault is highly model dependent.

Table 1 lists all the model statistics. The two models with the least postfit NRMS are models D and F, both of which require a second fault west of the primary fault. A

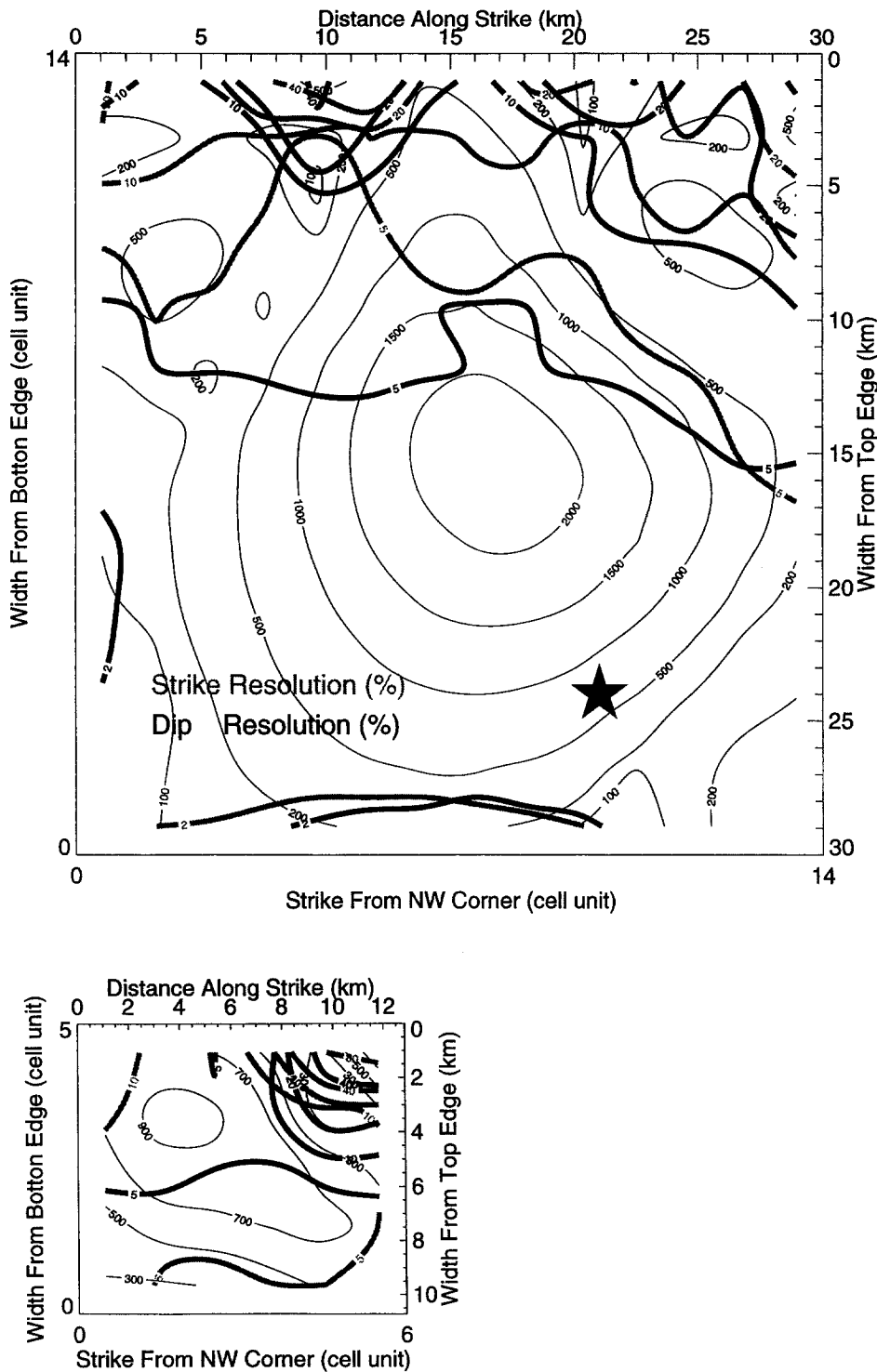


Figure 6. Resolution and total slip contours of model F. The gray and black thick contours indicate the percentages of the resolutions of the strike and dip-slip components, respectively. The generally low resolution results from strong smoothing in our model. The strike and dip components are about equally resolved. The thin contour lines illustrate the amplitude of the slip, peaked at 2.2 m at a depth of about 12 km at the primary fault and 0.9 m at a depth of about 3 km at the secondary fault.

close examination of the postfit residuals (Figs. 7 and 8) reveals why the second fault plane improves the fit so much. The improvements are made mainly in the western part of the network, where model F fits much better at sites U145, CHAT, CALA, and 0094 than model E. Such improvements suggest that there has been shallow depth deformation in the neighborhood west of the epicenter. It is difficult to rule out completely the possibility of monument instabilities, but the

significant improvement of fit for model F at a group of sites suggests that significant folding or creeping is plausible. On the other hand, the NRMS residual of model F also suggests that some part of the data remain unexplained by the model. Residuals may be attributed to more extensive folding or creeping, aftershock disturbance, or local monument instabilities. A close examination of the aftershock sequence reveals that several significant aftershocks ($M > 5.0$) occurred

Table 1
Dislocation Models

| Model | Earth Model | No. of Fault Surfaces | Slip Distribution | Aftershock Plane? | No. of Parameters | Postfit χ^2 | Postfit NRMS |
|-------|-------------|-----------------------|-------------------|-------------------|-------------------|------------------|--------------|
| A | uniform | 1 | uniform | no | 9 | 649.3 | 1.93 |
| B | uniform | 1 | uniform | yes | 6 | 1304.8 | 2.72 |
| C | layered | 1 | uniform | no | 9 | 718.2 | 2.03 |
| D | uniform | 2 | uniform | yes | 15 | 366.8 | 1.48 |
| E | uniform | 1 | varied | yes | 26.3 | 383.8 | 1.57 |
| F | uniform | 2 | varied | yes | 35.6 | 258.6 | 1.33 |

off the primary fault plane. One of them is an M 5.1 shallow event, which occurred 29 January 1994, located right beneath the station PICO. A postseismic study by Donnellan *et al.* (1994) revealed that this station was displaced 40 mm to the south by the aftershock. The stations significantly affected by this event are three sites located close to each other: PICO, SAFE, and SAFR. Because the GPS measurements made after this aftershock have been excluded from the analysis (Hudnut *et al.*, 1996), we expect no significant influence of this event to any site in our network. It is interesting, however, that many aftershocks occurred west of the epicentral area, with a number of magnitude 5 or larger events having occurred within the week after the mainshock, in the vicinity of our resolved second fault. However, the seismic moment release of those aftershocks is about five times smaller than our second fault would predict; introducing the magnitude 5 and greater aftershocks that have occurred in this region into modeling cannot fit the data nearly as well as model F does. Nevertheless, such aftershock behavior suggests that the upper crust in the region became highly fractured, possibly suffering both seismic and aseismic deformation. Thus, although we have included one more fault plane in our model and one more term in our error model to account for the near-field inelastic disturbance, in this particular area, we may still be underestimating the errors caused by such an effect.

Discussion

Major conclusions are summarized in the Abstract and Table 1 and will not be repeated here.

This article utilizes data from a joint project described in Hudnut *et al.* (1996). We collaborated directly with Hudnut *et al.* (1996) to assure agreement among all authors on the displacement vectors that we take as input data for this study. The interpretation of those data and the dislocation models presented here were computed independently. Differences between the two approaches include the assumed error model, the type of prior information used to assure a physically reasonable model such as the fault configurations and earth structure, the relative weighting given to “smoothness” and fit to geodetic data, and the algorithms used to adjust the nonlinear parameters. Despite the dissimilarity in methodology, the general agreement of our model E with

the distributed slip model of Hudnut *et al.* is strong evidence that the conclusions follow from the data rather than arbitrary choices in parameterizing the model. The major difference between our models E and F is that model E has about 0.8-m oblique/reverse faulting at the northwest corner of the fault plane whereas model F does not. The distributed slip model of Hudnut *et al.* (1996) demonstrates greater than 0.5-m normal faulting there. The significant surface slip in model E and in the model of Hudnut *et al.* are resulted mainly from fitting the displacement vector at station NEWH. The difference in the slip direction predicted by the two models is probably due to differences in the assumed geometry. The absence of such a significant surface slip in model F suggests that the displacement at station NEWH can also be explained by slip along faults located further south.

It is worthwhile to compare our model F with the results from strong-motion studies, since one reflects the static dislocation field and the other reveals the dynamic rupture process of the earthquake. The strong-motion results given by Wald *et al.* (this issue) show a quite heterogeneous slip pattern, with about 1.5- to 2.0-m slip near the hypocenter (at a depth of about 17 km) southeast of the fault plane and about 2-m maximum slip at the central and central-west area of the fault plane (at a depth of about 12 km). The amount of slip in the area between the high peaks is about 1 m in general. There is very little slip above a depth of 8 km. However, model F shows a rather smoothed slip pattern, with a maximum slip of 2.2 m at the center of the fault plane at a depth of 12 km. Wald *et al.* (1996) also modeled a subset of the GPS data used for this study; their result shows a similar pattern to ours.

The dissimilarity of the strong-motion and GPS results suggests complexity of the fault plane rupture in both space and time. Because the strong-motion data are sensitive to the high-frequency (about 1.0 to 10 Hz) co-seismic rupture signals, its result may well reflect the rupture pattern after the first few seconds of the earthquake. The GPS result, on the other hand, describes a somewhat averaged permanent slip pattern, which includes all the aftershock slips prior to the postearthquake GPS occupation. With all the potential differences in mind, we find that the two results still have the most significant feature in common, i.e., the largest slip of about 2 m at a depth of about 12 km. The significant slip near the hypocenter detected by strong motion, if true, prob-

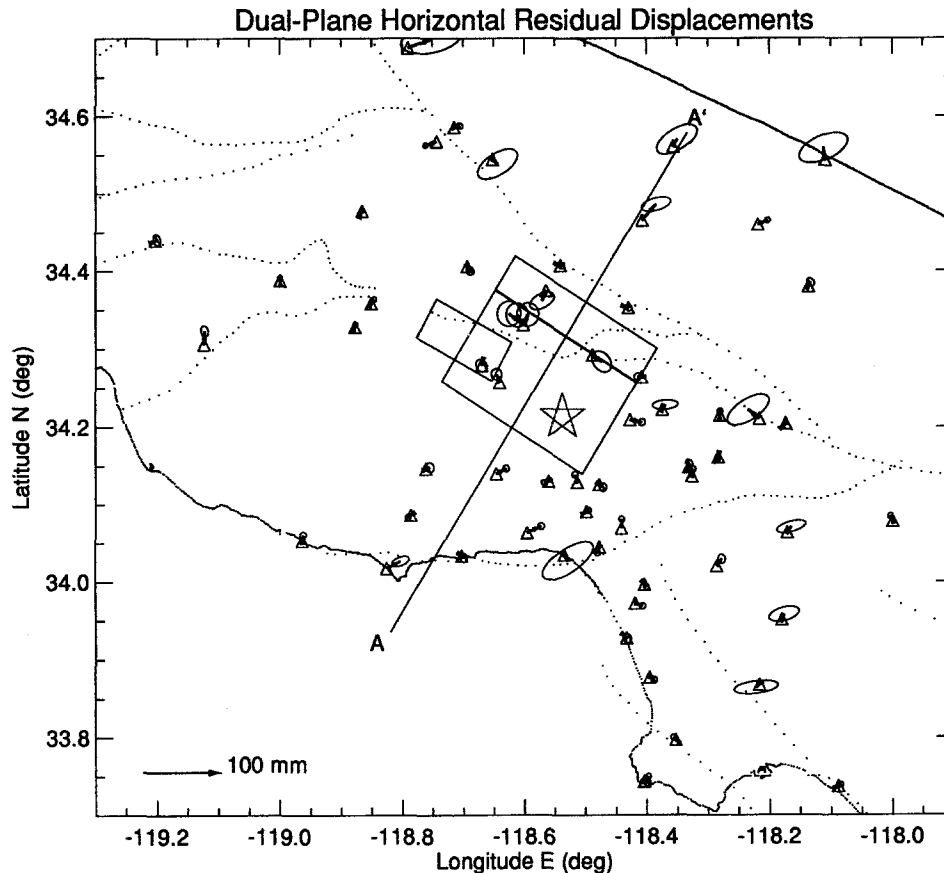


Figure 7. Horizontal residual displacements of model F. Otherwise, same as Figure 2.

ably is too deep to be convincingly detected by GPS, and the smoothing applied to our model tends to iron out such deep-seated features. Also, the shallow faulting detected by GPS is probably caused by postseismic deformation that would not be picked up by strong motion.

The second fault plane of our model F may well be a surrogate for a complex of additional faults that fractured at the time of the mainshock or aseismic deformation stimulated by new stress imposed on the area by the mainshock. Geodetic studies (Donnellan *et al.*, 1993a, 1993b) showed that the Ventura Basin is under fast convergence, which takes place aseismically. Our second fault plane is located at the east end of the Ventura Basin, where there has been active deformation at depth. It would not be surprising if the Northridge earthquake triggered immediate acceleration of that process, although it is not easy to pin down the exact location of the fault. The inferred seismic moment released on the second fault is approximately 14% of that released on the main fault. This contribution is small enough that the moment observed seismically (Jones *et al.*, 1994; Dreger, 1994) might include only that on the primary fault or the sum of the moments on the main and second faults; as both the total seismic moments of 1.5×10^{19} N-m or the moment release of 1.34×10^{19} N-m for the primary fault only are consistent with the strong-motion result (1.4×10^{19} N-m;

Wald *et al.*, this issue). Without specific simulation of the seismic data using a two-fault model, it is difficult to say whether our model is compatible with the long-period seismic radiation. Nothing in our model would explain the short-period content of the strong-motion records (e.g., Wald *et al.*, this issue); thus, a more detailed model to fit the combined datasets would be appropriate.

Our varied slip results place the upper boundary of the meter-level co-seismic rupture at a depth of about 5 km. This claim is different from a previous finding by Jones *et al.* (1994) based on seismological and geodetic data (an early version of some of the GPS data we use for this study). They concluded that the slip was confined below a depth of 8 km and did not penetrate the fault plane of the 1971 Sylmar earthquake. We find that there is still significant slip above the intersection depth of the two fault planes, at a depth of about 7 km. However, we cannot exclude the possibility that the significant slip we find above the Sylmar earthquake fault plane might come from aftershocks occurring prior to our postearthquake GPS occupation.

Acknowledgments

This article uses data from a joint project described in Hudnut *et al.* (this issue). We would like to thank the authors of that article, Ken Hudnut,

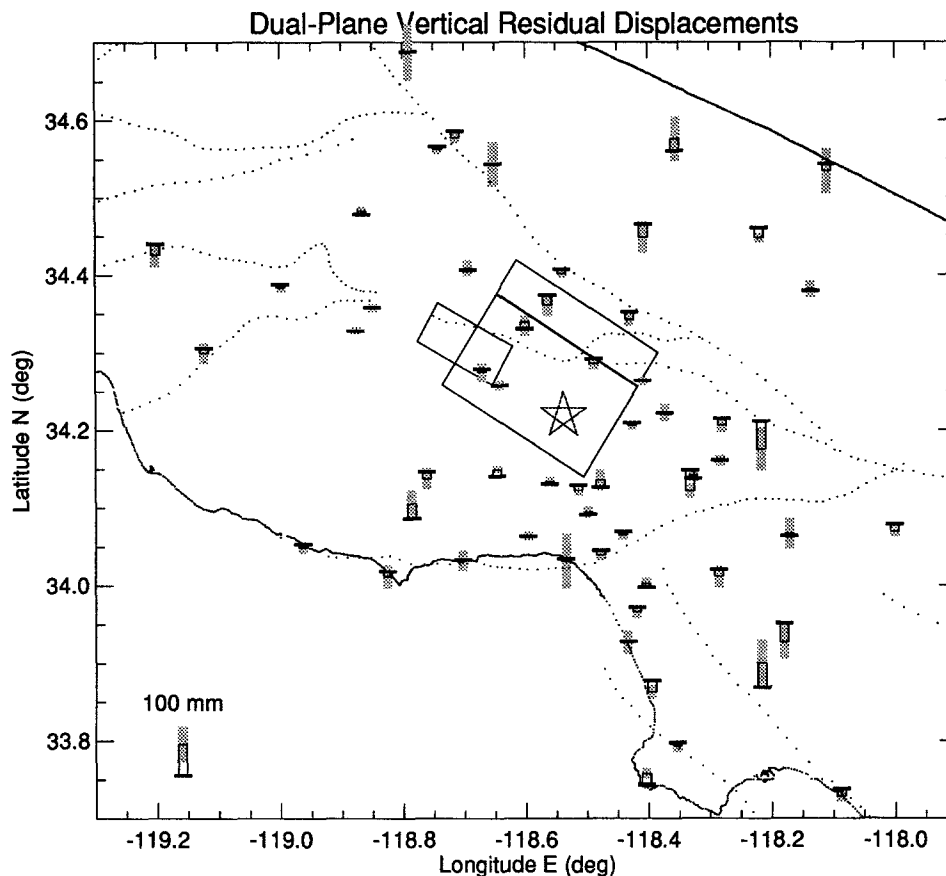


Figure 8. Vertical residual displacements of model F. Otherwise, same as Figure 3.

Mark Murray, Simon McClusky, Robert King, Tom Herring, Brad Hager, Yanjie Feng, Peng Fang, Andrea Donnellan, and Yehuda Bock, who contributed from field data collection, to data processing, to co-seismic displacement modeling. We would also like to thank people from the National Geodetic Survey, the Caltrans District 7 and Headquarters, Los Angeles County, and City of Los Angeles, particularly to Don D'Onofrio, Jay Satalich, Larry Fenske, Bob Packard, Bob Reader, and many others, who have helped with organizing and conducting the field surveys and with making the GPS data available. We are very grateful to Stephen Salyards for his assistance in data archiving and to Danan Dong for his sharing the FONDA software with us. Special thanks goes to Steven Ward for his assistance to our coding of forward dislocation modeling in a layered earth, from formula derivation to programming tips. We are also grateful to the editors K. Aki and L. Teng and an anonymous reviewer for their helpful comments. This work has been supported by the National Science Foundation, the United States Geological Survey, through the Southern California Earthquake Center, Grant 608816 and Southern California Earthquake Center Publication No. 202.

References

- Davis, T. L. and J. S. Namson (1994). A balanced cross-section of the 1994 Northridge earthquake, southern California, *Nature* **372**, 167–169.
- Davis, T. L., J. Namson, and R. F. Yerkes (1989). A cross section of the Los Angeles area: seismically active fold and thrust belt, the 1987 Whittier Narrows earthquake, and earthquake hazard, *J. Geophys. Res.* **94**, 9644–9664.
- Dong, D. (1993). The Horizontal velocity field in southern California from a combination of terrestrial and space-geodetic data, *Ph.D. Thesis*, Massachusetts Institute of Technology, Cambridge.
- Donnellan, A., G. A. Lyzenga, and B. H. Hager (1994). GPS measurement of postseismic deformation associated with the Northridge earthquake (abstract), *EOS* **75**, 166.
- Donnellan, A., R. H. Hager, R. W. King, and T. A. Herring (1993a). Geodetic measurement of deformation in the Ventura Basin region, southern California, *J. Geophys. Res.* **98**, 21727–21739.
- Donnellan, A., B. Hager, and R. King (1993b). Discrepancy between geological and geodetic deformation rates in the Ventura basin, *Nature* **366**, 333–336.
- Dreger, D. S. (1994). Empirical Green's function study of the January 17, 1994 Northridge, California earthquake, *Geophys. Res. Lett.* **21**, 2633–2636.
- Ekstrom, G., R. Stein, J. Eaton, and D. Eberhart-Phillips (1992). Seismicity and geometry of a 110-km-long blind thrust fault, 1, The 1985 Kettleman Hills, Calif. earthquake, *J. Geophys. Res.* **97**, 4843–4864.
- Herring, T. A. (1993). GLOBK: Global Kalman Filter VLBI and GPS analysis program, v.3.1, Massachusetts Institute of Technology, Cambridge.
- Hudnut, K. W., Z. Shen, M. Murray, S. McClusky, R. King, T. Herring, B. Hager, Y. Feng, P. Fang, A. Donnellan, and Y. Bock (1996). Co-seismic displacements of the 1994 Northridge, California, earthquake, *Bull. Seism. Soc. Am.* **86**, no. 1B, S19–S36.
- Jackson, D. D. (1979). The use of a priori data to resolve non-uniqueness in linear inversion, *Geophys. J. R. Astr. Soc.* **57**, 137–157.
- Jones, L. M., K. Aki, D. Boore, M. Celebi, A. Donnellan, J. Hall, R. Harris, E. Hauksson, T. Heaton, S. Hough, K. Hudnut, K. Hutton, M. Johnston, W. Joyner, H. Kanamori, G. Marshall, A. Michael, J. Mori, M. Murray, D. Ponti, P. Reasenberg, D. Schwartz, L. Seeber, A. Shakal, R. Simpson, H. Thio, J. Tinsley, M. Todorovska, M. Trifunac, D. Wald, and M. L. Zoback (1994). The magnitude 6.7 Northridge, California, earthquake of 17 January 1994, *Science* **266**, 389–397.

- King, R. W. and Y. Bock (1993). Documentation for the MIT GPS analysis software: GAMIT, Massachusetts Institute of Technology, Cambridge.
- Mori, J., D. J. Wald, and R. L. Wesson (1995). Overlapping fault planes of the 1971 San Fernando and 1994 Northridge, California, earthquake, *Geophys. Res. Lett.* **22**, 1033–1036.
- Okada, Y. (1985). Surface deformation due to shear and tensile faults in a half-space, *Bull. Seism. Soc. Am.* **75**, 1135–1154.
- Shen, Z.-K., D. D. Jackson, and B. X. Ge (1995). Crustal deformation across and beyond the Los Angeles basin from geodetic measurements, submitted to *J. Geophys. Res.*
- Song, X., L. E. Jones, and D. V. Helmberger (1994). Source characteristics of the January 17, 1994 Northridge, California earthquake from regional broadband modeling, Program for Northridge Abstracts, the 89th Annual Meeting of the Seismological Society of America.
- Thio, H. K. and H. Kanamori (1994). Moment tensor solutions for the Northridge earthquake sequence, Program for Northridge Abstracts, the 89th Annual Meeting of the Seismological Society of America.
- Wald, D. J., T. H. Heaton, and K. W. Hudnut (1996). The slip history of the 1994 Northridge, California, earthquake determined from strong-motion, teleseismic, GPS, and leveling data, *Bull. Seism. Soc. Am.* **86**, no. 1B, S49–S70.
- Ward, S. N. (1984). A note on lithospheric bending calculations, *Geophys. J. R. Astr. Soc.* **78**, 241–253.
- Zhang, J., S. Tsuboi, and T. Lay (1994). Analysis of broadband far-field seismic data for the January 17, 1994 Northridge, California earthquake, *EOS* **75**, no. 44, 171.
- Zhao, L.-S. (1994). Regional waveform modeling of the main shock of 17 January 1994 Northridge, California earthquakes, Program for Northridge Abstracts, the 89th Annual Meeting of the Seismological Society of America.
- Zhou, H. (1995). Focal depth bias in underestimated velocity models, submitted to *Bull. Seism. Soc. Am.*
- Yeats, R. S. and G. J. Huftile (1995). The Oak Ridge fault system and the 1994 Northridge earthquake, *Nature* **373**, 418–420.
- Yeats, R. S. (1993). Converging more slowly, *Nature* **366**, 299–301.

Department of Earth and Space Sciences
 University of California, Los Angeles
 Los Angeles, California 90024-1567
 (Z.-K.S., B.X.G., D.D.J., D.P., L.-Y.S.)

New Jersey Department of Transportation
 Geodetic Survey
 Trenton, New Jersey 08625-0600
 (M.C.)

Manuscript received 26 January 1995.